HHS Public Access

Author manuscript

Microcirculation. Author manuscript; available in PMC 2018 November 01.

Published in final edited form as:

Microcirculation. 2017 November ; 24(8): . doi:10.1111/micc.12393.

Agent-based Computational Model of Retinal Angiogenesis Simulates Microvascular Network Morphology as a Function of Pericyte Coverage

Joseph Walpole, MD, PhD[*], **Feilim Mac Gabhann, PhD**[‡], **Shayn M Peirce, PhD**[*], and **John C Chappell, PhD**[†]

[*]University of Virginia Department of Biomedical Engineering

[†]Virginia Tech Carilion Research Institute, Department of Biomedical Engineering and Mechanics

[‡]Johns Hopkins University Department of Biomedical Engineering

Abstract

Objective—Define a role for perivascular cells during developmental retinal angiogenesis in the context of endothelial cell Notch1-DLL4 signaling at the multicellular network level.

Methods—The retinal vasculature is highly sensitive to growth factor mediated intercellular signaling. Although endothelial cell signaling has been explored in detail, it remains unclear how pericytes function to modulate these signals that lead to a diverse set of vascular network patterns in health and disease. We have developed an agent-based model of retinal angiogenesis that incorporates both endothelial cells and pericytes to investigate the formation of vascular network patterns as a function of pericyte coverage. We use our model to test the hypothesis that pericytes modulate Notch1-DLL4 signaling in endothelial cell-endothelial cell interactions.

Results—ABM simulations that include pericytes more accurately predict experimentally observed vascular network morphologies than simulations that lack pericytes, suggesting that pericytes may influence sprouting behaviors through physical blockade of endothelial intercellular connections.

Conclusion—This study supports a role for pericytes as a physical buffer to signal propagation during vascular network formation – a barrier that may be important for generating healthy microvascular network patterns.

Keywords

Agent Based Model; Angiogenesis; Pericyte; Endothelial Cell; Retina

Introduction

The developing murine retinal vasculature has long been a mainstay model for studies that explore physiological and pathological angiogenesis [1]. Mouse pups are born before their retinas are fully formed, with a stereotyped and conserved pattern of vascular patterning

Corresponding Author: Shayn M Peirce, smp6p@virginia.edu.

occurring over the course of approximately two weeks [2]. During the first 7 days of postnatal development, an angiogenic front of endothelial cells (ECs) grow along a template of astrocytes, beginning from the optic nerve and radiating outward to the distal retinal edge [3-5]. Over time, the angiogenic front advances, with the older, more proximal vasculature beginning a process of maturation – development of arterial/venous polarity, growth of vessels that penetrate deeper into the retinal tissue, and capillary rarefaction.

Throughout this process, pericytes (PCs), cells that enwrap endothelial cells, are maintained in close proximity to the EC network (Figure 1) [6]. Throughout the body, pericytes have been shown to affect vascular permeability [7, 8], capillary sprouting [9], capillary diameter [10], and leukocyte trafficking [11]. Loss of PCs in the eye plays a key role in the pathogenesis of several human eye diseases, notably proliferative diabetic retinopathy (DR), retinopathy of prematurity, and cancer-associated retinopathy [12-17]. We have previously published evidence suggesting that an adipose-derived stem cell treatment may in fact reverse PC loss in multiple murine models of DR, reducing capillary loss [18]. Further, Simonavicius et al. 2012 demonstrated pericyte-induced endothelial cell apoptosis through an Endosialin-mediated pathway, while Benedito et al. 2009 proposes a role for non-endothelial sources of DLL4 that may affect vessel sprouting [19, 20]. These studies reveal a potential interplay between the Notch1-DLL4 EC signaling axis and PC function in the developing vasculature.

Despite the prevalence of retinal models of angiogenesis and a key role for PCs in retinal vascular development and health, much is still unknown about the function of PCs during vascular development. Specifically, the canonical Notch1-DLL4 signaling pathway in ECs has been studied in great detail [21-24], yet little has been done to elucidate how PCs may modulate that signaling axis. Computational models of the vascular endothelial growth factor receptor (VEGFR) and its effects on EC Notch1-DLL4 signaling have also been used to investigate endothelial behavior in angiogenic sprouts and vessel networks, but they do not explicitly account for putative effects of PCs during angiogenesis [25-29]. Therefore, we have developed an agent-based model (ABM) for simulating EC and PC interactions at the angiogenic front during retinal vascular development.

Our ABM incorporates Notch1-DLL4 intercellular signaling between ECs, allowing for signal propagation throughout a multicellular network. EC directed chemotaxis is achieved through a stochastic model of VEGFR binding kinetics that accounts for competition between pro-angiogenic VEGFR2 and anti-angiogenic VEGFR1 [24, 30]. A procedurally generated astrocyte network is included as the source of VEGF [1, 4, 5]. Our novel application of Minkowski functionals to experimental and simulated angiogenic networks allows us to quantitatively compare the network patterns of ABM-generated EC networks with images of actual angiogenic fronts taken from murine retinas [2]. Minkowski analysis is an integral-geometry method for quantifying morphologies of binary images using a minimum of 3 functionals (the minimum number of functionals required to describe an image is one more than the total dimensionality of the image – thus a two dimensional image requires three functionals) [31]. Milde et al. 2008 used this analysis to describe the normal developmental patterns of murine retinal vasculature across several postnatal days and we are expanding upon this analysis to compare simulated retinae to in vivo retinal images.

Our results suggest that the presence of PCs alone, without any direct signaling to ECs, affects network patterning. As compared to simulated networks comprised of only ECs, simulated networks with PCs more closely match the geometric properties of physiologic retinal vascular networks. Further, this effect cannot be replicated solely by increasing or decreasing the density of ECs in the network – PCs must be present in the simulation to best match physiologic network patterns. This supports a role for PCs as signaling "buffers" – spacing ECs to limit their intercellular contacts and preventing aberrant vessel growth due to inefficient or inaccurate intercellular communication.

Materials and Methods

Retinal Dissection and Immunohistochemistry

All procedures were approved by the Institutional Animal Care and Use Committee (IACUC) at the University of Virginia and Virginia Tech Carillion Research Institute. Adult C57bl/6 mice were obtained from Jackson Laboratories and maintained in breeding pairs. At postnatal day 3 (P3) mouse retinas were dissected as previously described [32].

Method 1 – Endothelial Cells and Astrocytes

For retinas used to quantitate P3 vascular morphology, eyes were enucleated and placed in a 0.4% paraformaldehyde solution for 7 minutes and then maintained in a phosphate buffered saline (PBS) solution for the remainder of dissection until slide mounting. While visualized using a Nikon SMZ1500 stereomicroscope, the sclera, lens, and hyaloid vasculature were removed and four relaxing incisions were made in a radially symmetric pattern around the posterior eyecup [33]. The remaining tissue was whole mounted on gelatin-coated slides.

Retinas were permeabilized with 1mg/mL Digitonin (Sigma-Aldrich, St. Louis, MO) in PBS for 1 hour followed by 3 washes with 1% bovine serum albumin (BSA) (Jackson ImmunoResearch, West Grove, PA) in PBS for 10 minutes each. Blocking of non-specific binding was accomplished by a 1 hour incubation in 1% BSA-PBS. Primary antibodies were diluted in 1% PBS-BSA (1:200 IB4, 1:1000 GFAP) and allowed to incubate on retinas for 1 hour followed by 3 washes with 1% BSA-PBS for 10 minutes each. All of the preceding procedures were carried out at room temperature. Secondary antibodies for GFAP were diluted at 1:300 in 1% BSA-PBS and allowed to incubate overnight at 4°C. Finally, retinas were washed 3 additional times with 1% BSA-PBS for at 10 minute intervals before applying a 50/50 glycerol/PBS solution and sealing slides with cover glass. Samples were viewed immediately, with less than 24 hours between initial retinal harvest and confocal imaging.

Visualization of retinal vascular ECs and astrocytes was achieved by immunohistochemical staining. *Griffonia simplicifolia* isolectin B4 (IB4) preconjugated to AlexaFluor-647 was used to identify ECs (Molecular Probes/Invitrogen/Life Technologies, Eugene, OR) [34]. Astrocytes were visualized by staining with a primary antibody against glial fibrillary acidic protein (GFAP, Dako/Agilent Technologies, Santa Clara, CA) [1, 2] and a secondary goat-anti-rabbit antibody conjugated to AlexaFluor 546 (Molecular Probes/Invitrogen/Life Technologies, Eugene, OR).

Method 2 – Endothelial Cells and Pericytes

Following whole animal perfusion with 0.5% paraformaldehyde (PFA), eyes were fixed by immersion in 2% PFA for 2 hours at room temperature. Retinae dissected from the whole eye were immersed in 100% cold ethanol (30 minutes) and re-hydrated with PBS containing 1% Triton X-100 (PBS-T) for 30 minutes at room temperature. Non-specific antibody binding sites were blocked by immersing retinae in 3% donkey serum in PBS-T for 1 hour at room temperature. Primary antibody incubation was performed in PBS-T overnight at 4°C with rat anti-platelet-endothelial cell adhesion molecule-1 (PECAM-1) (BD Biosciences, MEC13.3, 1:200) and rabbit anti-neural glial antigen-2 (NG2) (EMD Millipore, 1:200). Secondary antibody incubation was also in PBS-T overnight at 4°C with donkey anti-rat AlexaFluor 647 (Jackson ImmunoResearch, 1:400) and donkey anti-rabbit AlexaFluor 568 (ThermoFisher Scientific, 1:400). Nuclei were labeled with DAPI (1:1000 in PBS-T, 30 minutes, room temperature). Retinae were washed 3×5 mins in PBS-T, flattened and mounted on slides in 50:50 PBS:glycerol with 1.5 coverslips. Using a Zeiss LSM 880 confocal microscope and a ×63 objective, 6-8 z-axis confocal scans of retina whole mounts were acquired and compressed.

Minkowski Analysis

Image processing was performed using ImageJ and MATLAB [35]. The Minkowski analysis is a method of quantitatively comparing images based on three geometric parameters: area, perimeter, and Euler coefficient. Milde et al. have previously demonstrated the efficacy of the Minkowski analysis for identifying blood vessel patterns in the murine retina as a function of postnatal age [2]. We have adapted the technique to study both astrocytic and endothelial cell networks at the leading edge of the developing vascular front in both experimental and *in silico* angiogenic networks.

To perform a Minkowski analysis, the image (either immunohistochemical staining or ABM-derived) was first filtered through a binary mask. Images were then skeletonized to reduce the network to a single pixel in diameter. The image area, perimeter, and Euler coefficient were then calculated as a function of the image dilation index (R). Through progressive image dilation a set of Minkowski functionals were generated that characterized the geometric properties of the original image. These image-processing steps are summarized in Figure S1. Area and perimeter values were normalized by the total area of the image to allow for comparison between images of different sizes and with different pixel dimensions.

ABM Temporal and Spatial Constraints

ABM simulations were implemented using NetLogo [36] and are available for download on the SimTK database. The total ABM simulation space was 0.087 mm^2 and is comprised of 5 μm^2 square pixels. Each EC and PC were assumed to maintain an average area of 500 μm^2 and therefore maintain a shape defined by 100 pixels (based on the assumption that in 2D only half of the total 1000 μm^2 surface area is available) [37]. Note that each of these 100-pixel membrane “patches” (a discrete agent element in NetLogo) define the membrane area and shape of the cells – after being instantiated as a square, cell shape during the simulations

was defined by membrane movements resulting from chemotaxis or cell-cell contacts (Figure 2).

The ABM time-step was set to 10 minutes to simulate cell behaviors that take place on the time scale of hours. Receptor binding and cell movement were iterated more than once per time-step. Specifically, cells had an opportunity to move (e.g. if a valid movement location was available) either 2 times (for quiescent ECs) or 4 times (for ECs with a tip cell phenotype). Tip cells have increased opportunities for movement to reflect their increased surveillance of nearby extracellular space. Receptor binding was estimated to steady-state by running 20 stochastic binding iterations per pixel. Simulations were run for a total of 80 time steps, or equivalently 13.3 hours to allow for vascular network extension at the angiogenic front.

Astrocyte Template Generation

Models were instantiated with a procedurally generated astrocyte template based on the Minkowski functionals of P3 murine retinal astrocytes (Figure S2). A variable number of starting pixel locations were randomly selected from the base of the model space. From each of these starting pixels, a new pixel "grew" within a 20-degree arc of the previous pixel's heading, extending the astrocyte template skeleton. At any time, branching events occurred with probability (P_{branch}), generating new paths. If forward movement converged upon an already existing path, the two branches converged and further progress was halted. The number of starting locations and P_{branch} were fit to generate an image with Minkowski functionals matching those of skeletonized astrocyte images from P3 murine retinas.

The finished ABM astrocyte template skeleton provided the only source of VEGF for the simulation with production and degradation rates of k_f and k_{deg}, respectively (Table 1) [38]. During each time-step, 40% of each pixel's VEGF concentration was equally distributed within its Moore neighborhood (the 8 adjacent pixels surrounding the diffusing pixel, effectively the closest neighbors within a single pixel radius [39]) to simulate diffusion (estimated based on model calibrations to use the Netlogo "diffuse" command).

Cell Types and Initial Conditions

Three different experimental conditions were evaluated: simulations with both ECs and PCs, simulations with only ECs, and simulations sparsely populated with ECs. After generating the astrocytic template, ECs and PCs were seeded into the simulation within 65 μm of the bottom to simulate the angiogenic front of a developing mouse retina. All simulations had at least 21 starting ECs plus 12 additional potential cell locations between the EC stalks. Simulations with ECs only had up to an additional 12 ECs (total of 32), while simulations with ECs and PCs had up to an additional 12 cells that each had a 75% chance of being PCs. This provided a starting template of pericyte coverage that paralleled our in vivo imaging observations (example image shown in Figure 1).

Finally, simulations with sparsely populated ECs had at least 21 starting ECs plus the possibility for 12 additional ECs, each with a probability of 25% of being added. This third experimental condition controls for effects of EC overcrowding in EC-only simulations. In these experiments, the total number of ECs was similar to those seen in simulations with

both ECs and PCs, but the total number of all cells was reduced to reflect the absence of PCs. These three simulation types are summarized in Figure 2.

Receptor Binding

In the ABM, ECs expressed two different forms of the VEGF receptor: VEGFR1 and VEGFR2. As was done previously by Mac Gabhann et al., receptor binding was approximated using a modified Gillespie algorithm for stochastic mass action kinetics [40-43]. Our modifications to the algorithm were designed to run to a steady state between each 10-minute time step and the time between each reaction was considered to be equivalent for 20 iterations. Reaction rates were defined based on the number of VEGF molecules (V), VEGFR1 (R1), VEGFR2 (R2), VEGF-VEGR1 complexes (VR1), and VEGF-VEGFR2 complexes (VR2):

$$r_{on}^{R2}=\frac{k_{on}^{R2}}{\mathrm{vol}\cdot N_A}\cdot V\cdot R2 \quad (1)$$

$$r_{on}^{R1}=\frac{k_{on}^{R1}}{\mathrm{vol}\cdot N_A}\cdot V\cdot R1 \quad (2)$$

and normalized by the reaction volume (vol, one pixel of area 5 μm^2 with pseudo height assumed to be 1 μm) and Avogadro's number (N_A). The receptor off rates were defined as:

$$r_{\mathrm{off}}^{R2}=k_{\mathrm{off}}^{R2}\cdot VR2 \quad (3)$$

$$r_{\mathrm{off}}^{R1}=k_{\mathrm{off}}^{R1}\cdot VR1 \quad (4)$$

The probability of receptor binding was thus a function of the on and off rates for both receptors at a given time, defined a P_{R1} and P_{R2} for receptors VEGFR1 and VEGFR2, respectively:

$$P_{R1}=\frac{r_{on}^{R1}}{r_{on}^{R1}+r_{\mathrm{off}}^{R1}} \quad (5)$$

$$P_{R2}=\frac{r_{on}^{R2}}{r_{on}^{R2}+r_{\mathrm{off}}^{R2}} \quad (6)$$

A random number (p_1) was generated and compared to the probabilities of binding to determine the binding reaction outcomes:

$$\left.\begin{array}{lcl} R1 & = & R1{+}1 \\ VR1 & = & VR1-1 \\ R2 & = & R2-1 \\ VR2 & = & VR2{+}1 \end{array}\right\} p_1{>}P_{R1}\,\hat{}\,p_1 \le P_{R2} \qquad \left.\begin{array}{lcl} R1 & = & R1-1 \\ VR1 & = & VR1{+}1 \\ R2 & = & R2{+}1 \\ VR2 & = & VR2-1 \end{array}\right\} p_1 \le P_{R1}\,\hat{}\,p_1{>}P_{R2}$$

$$\left.\begin{array}{lcl} V & = & V-2 \\ R1 & = & R1-1 \\ VR1 & = & VR1{+}1 \\ R2 & = & R2-1 \\ VR2 & = & VR2{+}1 \end{array}\right\} p_1 \le P_{R1}\,\hat{}\,p_1 \le P_{R2} \qquad \left.\begin{array}{lcl} V & = & V{+}2 \\ R1 & = & R1{+}1 \\ VR1 & = & VR1-1 \\ R2 & = & R2{+}1 \\ VR2 & = & VR2-1 \end{array}\right\} p_1{>}P_{R1}\,\hat{}\,p_1{>}P_{R2} \quad (7)$$

Integration of new VEGFR2s and internalization of receptors or receptor complexes followed a similar algorithm whereby the insertion rate (sR) was initially balanced with the internalization rate (k_{int}) given 100 receptors at the cell surface:

$$sR{=}100 \cdot k_{\text{int}} \quad (8)$$

This was then modified to reduce the insertion rate as a function of the Notch1 activity in the cell:

$$\widehat{sR}{=}sR \cdot \left(1 - \frac{\text{Notch}}{\text{Notch}_{\text{max}}}\right) \quad (9)$$

such that when Notch1 activity is maximal, no new VEGFR2 were expressed on the surface. $Notch_{max}$ was defined as a relative maximum for each simulation based on the cell with the highest amount of Notch1 activity. Finally, the probability of incorporating a new receptor (Pinsert) was defined as:

$$P_{\text{insert}}{=}\frac{\widehat{sR}}{\widehat{sR}{+}k_{\text{int}} \cdot (R2{+}VR2)} \quad (10)$$

and a random number (p_2) was generated to determine the VEGFR2 turnover at the cell surface:

$$\begin{array}{lcl} R2 & = & R2-1 \\ & & or \\ VR2 & = & VR2-1 \end{array} \; p_2 \le P_{\text{insert}}\; R2{=}R2{+}1\}p_2{>}P_{\text{insert}} \quad (11)$$

Note that there is an equal probability of removing either VEGFR2 (R2) or a VEGF-VEGFR2 complex (VR2) given that $p_2 < P_{insert}$. VEGFR1 was assumed to be maintained at a steady state concentration, such that the insertion and internalization rates are equal – thus, VEGFR1 surface turnover is not explicitly simulated.

Intercellular Signaling

ECs were capable of communicating via a simulated Notch1-DLL4 mechanism, allowing for cells to modulate the insertion rate of new VEGFR2 molecules in their neighbors per equation 9. The canonical Delta-like protein 4 interaction with Notch1 in vascular development has been well studied. Briefly, VEGFR2 increases DLL4 expression which in turn drives increased Notch1 expression in neighboring cells – this balance effectively "activates" ($DLL4^{high}$) tip cells while "deactivating" ($Notch1^{high}$) stalk cells to allow for vascular patterning [21, 44-46]. Each time step, ECs sum the DLL4 activity of their neighboring ECs (defined as any non-self EC within a Moore neighborhood) to determine their own Notch1 activity as defined by equation 12:

$$\mathrm{Notch1}_{t+1} = \left(\alpha + \sum \mathrm{DLL4}_t\right) \quad (12)$$

where α is the Notch transfer coefficient. This α value scales the current DLL4 input from neighboring ECs such that increasing α increases the Notch1 activity; conversely, a value of $\alpha = 0$ decouples the system and simulates a loss of Notch1-DLL4 signaling.

Simulated Cell Behaviors

The primary cellular behaviors and a process diagram of their implementation in the ABM can be found in Figure 2. ECs and PCs both maintained a connection with cells that they were already contacting. Importantly, loss of all cell contacts was a condition for cell death – if ECs completely lost contact with any other ECs or PCs they underwent apoptosis [47, 48]. Similarly, if a PC lost contact with all neighboring ECs they also underwent apoptosis. Note that cell contacts are defined by the number of membrane patches adjacent to membrane patches belonging to other cells.

ECs were also capable of chemotaxis in response to VEGF [49]. Specifically, when an EC moved, it surveyed neighboring empty spaces (i.e. not already occupied by an EC or PC) and moved towards the one with the highest VEGF concentration [50-52]. ECs transitioned from a quiescent to a tip cell phenotype if the number of ligated VEGFR2 Molecules (VR2 in Equation 7) exceeded a threshold value of β. If VR2 dropped below β, the EC returned to a quiescent state. ECs with the tip cell phenotype had increased motility, which was simulated by doubling the number of migration attempts per time-step over quiescent ECs [50]. Du et al. 2016 have demonstrated that tip cells are able to surveil an area more than 1.5 times greater than stalk cells over the same time period in culture, supporting this increased motility[53].

As cells migrated away from the initial starting positions, new ECs and PCs were added to simulate the growth of cells trailing the leading edge of the angiogenic front [54]. The placement of these new cells followed the same rule set as the placement of the t_0 cells. In our simulations, cell division does not occur at the leading edge of the angiogenic front. Probabilities of cell placement and model instantiation steps are summarized in Figure 2.

A total of 160 different α and β parameter combinations with 10 replicates for each were completed for each of the three initial conditions (EC only, EC and PC, Sparse EC). These simulations provided the dataset for the analyses presented in this manuscript.

Statistics and Linear Regression

Confidence intervals, one-way analysis of variance (ANOVA), partial least squares regression analysis, and calculation of associated root mean squared error (RMSE) were performed using GraphPad Prism version 5.0d for Mac OSX and MATLAB. Unless otherwise stated, significance was asserted at $P \leq 0.01$

Results

ABM Simulations Recapitulate Experimentally Observed Retinal Vascular Patterns

The first simulation case condition to consider is the baseline ABM in which ECs and PCs are present, as is seen in normal retinal development. Recall that the astrocytic template and cell positions were stochastically generated, such that each replicate had a different starting configuration (see Supplemental Results and Figure S1).

In figure 3 we examine a simplified network of only 12 ECs and 3 PCs to illustrate the association between vascular network morphology and calculated Minkowski Functionals. Vascular networks grow over time and are then analyzed as a function of image dilation (R). The overall shape of the area functionals are similar, however as the network expands the initial values of area increase correspondingly and have a shallower slope. Conversely, the perimeter functional has a smaller starting value as a function of time, reflecting a more continuous network perimeter that does not change significantly with image dilation. Finally, the Euler number demonstrates fewer “holes” at t0 (as evidenced by the positive value), while later time points have more “holes” (evidenced by negative initial values) which are reflective of vascular loops.

ABM Simulations of Retinal Microvascular Network Patterns in the Presence and Absence of PCs

To compare the ABM simulations for each case (EC only, EC + PC, and sparse EC) and to evaluate their abilities to recapitulate the microvascular network patterns observed in the developing murine retina, the Minkowski functionals for ABM-generated EC networks were compared to the Minkowski functionals generated for immunohistochemically stained P3 mouse retinas. A total of 160 different combinations of α and β were tested with 10 replicate simulations being performed for each combination using each of the three experimental conditions. This produced an ensemble of 4,800 ABM EC network images, each of which was characterized in an automated manner using Minkowski functionals.

The similarity between the ABM-generated networks and murine P3 retinas was evaluated by determining whether or not the Minkowski functionals for the ABM-generated networks fell within the 95% confidence interval (CI) of the Minkowski functionals for the actual P3 retinae. This similarity criterion allowed us to quantitatively assess the "performance" of the ABM; better performance was indicated by having more data points that fell within the 95% CI. ABM performance for all parameter combinations and all experimental conditions is shown in Figure 5A-D, and an example of single parameter analysis is shown in Figure 4. Simulations with ECs and PCs greatly outperformed both other cell configurations when assessing the AREA functional (Figure 5A). Similarly, with respect to the EULER CHARACTERISTIC functional (a measure of closed loops within the network), simulations with both ECs and PCs also exhibited the best performance (Figure 5C). In contrast, ABM performance as characterized by the PERIMETER functional was not distinguishable between simulations with PC and EC, sparse EC, or EC only, and marginally better performance was seen in simulations with only ECs (Figure 5B).

Sparsely populated EC networks performed modestly across all Minkowski functionals. For only a few alpha and beta combinations did they outperform networks with both ECs and PCs, but for both the AREA functional and EULER CHARACTERISTIC functional, sparsely populated EC networks clearly performed better than more densely populated EC-only networks.

Finally, a cumulative performance score was generated by summing each of the Minkowski functionals (Figures 5E). This score mirrors what is described above, with ABM simulations of both ECs and PCs having the best overall performance, followed by sparsely populated EC simulations. No parameter combination for ABM simulations with only ECs performed better than the simulations with sparse ECs or both ECs and PCs.

Inclusion of Pericytes in the ABM Produces Simulated Networks with Greater Branching and Larger Loops

The slope of the Minkowski functionals provides additional insight into microvascular network pattern. As shown in an example analysis (Figure 4), simulations with ECs and PCs have a more gradual rise in their AREA functional as compared to other simulation types. Across all 160 parameter combinations, simulations with ECs and PCs had a significantly smaller slope within the first 10 image dilations (ANOVA $p<0.01$, average RMSE = 0.018, Figure 6A), which is characteristic of a network that, on the whole, has fewer intercellular spaces and less tortuosity.

Similarly, the PERIMETER functional demonstrates a shallower slope in the example case for the simulation with ECs and PCs (Figure 4). This was, again, true across all parameter combinations, where simulations having both ECs and PCs had a significantly less negative slope compared to all simulations with only ECs (ANOVA $p<0.01$, RMSE = 9.98E-4, Figure 6B). A shallow slope for the PERIMETER functional is associated with more simple structures, lacking the complexity associated with vessel tortuosity.

A branch point analysis of simulated and native P3 retinas demonstrates that the ABM-generated networks typically have fewer overall branch points (Figure 6C). Exemplar

images of skeletonized cell networks reveal that native network have more branch points with fewer spokes per branch point as compared to simulated networks (Figure 5F). These exemplar images also demonstrate an increased number of blind-ended branches and fewer vascular loops in ABM simulations without PCs, in agreement with the Minkowski Functionals.

Assigning an average slope value to the EULER CHARACTERISTIC functional was more challenging due in part to the high variability in some datasets, exemplified by the EC-only simulations (Figure 4). This generated large residuals (average RMSE = 0.95 for the EULER CHARACTERISTIC functional) relative to the observed data, rendering associated linear fits unreliable. Large negative slopes for the EULER CHARACTERISTIC functional are indicative of high-density blind-ended loops, which was the trend for simulations with only ECs. Small positive slopes, as seen in the EC and PC simulations, suggest the presence of lacunae (vascular loops) of various sizes that gradually close as the image is dilated. Both of these trends were observed in the example EULER CHARACTERISTIC functional graph (Figure 6D); however, we were unable to identify any significant differences between ABM-generated networks with ECs only, sparse ECs, or PCs and ECs.

Pericytes Promote Polarization of Notch1-DLL4 Signaling in Simulated Vascular Networks

Qualitative analysis of relative Notch1-DLL4 signal strength in simulated vascular networks demonstrate an increase in overall signal strength in EC-Only networks (Figure 7Biii-iv). Notably, loss of pericyte coverage caused broad upregulation of signal across the angiogenic front and extending proximally to the stalk cell region. Networks with PCs show an alternating pattern of $Notch1^{high}$ and $DLL4^{high}$ signal at the angiogenic front without proximal propagation (7Bi-ii).

Discussion

In this paper, our objective was to develop a novel ABM of developmental retinal angiogenesis in order to test the hypothesis that pericytes affect the Notch1-DLL4 landscape of endothelial cells, resulting in vascular network-scale morphology changes. This effect was seen as an emergent phenomenon whereby pericytes exert an indirect “buffering” effect on endothelial cell signaling during capillary sprouting that affects microvascular network patterning. Our ABM of murine retinal angiogenesis focused on cellular behaviors at the angiogenic front – a dynamic region of cell growth that moves across the developing retina over time during post-natal development. We explicitly simulated receptor binding, intercellular communication via Notch1-DLL4 pathways, and chemotaxis. Additionally, we incorporated PCs that served as buffers to intercellular signaling – while PCs exerted no direct effect on EC behavior, they limited the number of intercellular connections that ECs could make by providing a physical barrier to EC movement. Subsequent formation of cellular networks and geometric patterns as quantitated by Minkowski functionals occurred purely as a result of these rules.

Our simulations predict that the mere presence of PCs as buffers to EC signaling and movement more closely recapitulates the actual network pattern of the angiogenic front than ABM simulations with only ECs (either densely or sparsely populated). Importantly, this

does not preclude direct effects of PCs on EC function and signaling – to the contrary, much has been written about the nuanced role that PCs play in maintaining EC function throughout the body [15, 19, 55-59]. This ABM asserts a more basic question: can PCs play a role in EC network signaling through their presence alone? Furthermore, is this a function of PCs or simply a feature of vascular networks with fewer ECs? Indeed, our results support a role for PCs in supporting EC network formation that is not achieved simply by reducing the number of total ECs (sparse EC simulations).

Our proposed model for this PC-EC interaction is shown in 7A, where the presence of pericytes helps maintain vascular network polarization and prevents diffuse Notch1-DLL4 pathway activation. Qualitatively, this model is supported by simulations which demonstrate an increase in overall Notch1-DLL4 signal strength in ECs at the angiogenic front without characteristic “salt and pepper” patterning (Figure 7B). This dysregulation of signaling results in an overall increase in vessel blind-ended branches and cell density due to increased simulated tip-cell activation and migration. Furthermore, simulations with PCs maintain Notch1 activation distally at the angiogenic front whereas EC-only simulations maintain strong signal activity in proximal stalk cell regions. Notably, several studies have previously imaged the developing retinal vasculature and demonstrated similar patterns of Notch1-DLL4 expression at the angiogenic front [60-62]. These studies demonstrate alternating patterns of Notch1 and DLL4 activity, with a preponderance of DLL4 at the leading edge while Notch1 expressed in the more quiescent regions – similar to our results in Figure 7. While these results are qualitative in nature, they are nonetheless provocative and would suggest a need for further investigation into Notch1-DLL4 signal propagation in multicellular networks and specifically those containing pericytes.

Importantly, our model is limited to demonstrating changes in Notch1-DLL4 signaling and network geometries – we cannot make predictions or comment on other signaling pathways which are also clearly involved in the patterning of endothelial cell networks. Our result of a $Notch1^{high}$-$DLL4^{high}$ cell and loss of signaling polarity across the endothelial cell network suggests that the presence of pericytes in simulations has an effect on Notch1-DLL4 pathway function, though the actual expression pattern in vivo may be different due to the effects of other signaling pathways.

Our geometric analysis using Minkowski functionals revealed that the microvascular network architecture of P3 retinas and ABM simulations with ECs and PCs agrees with our understanding of vessel networks at the angiogenic front. As described by the slopes of the AREA and PERIMETER functionals (Figures 5D, E), these simulated vessel networks were characterized by having many branches and asymmetrically sized lacunae. While PCs have not yet been described to directly contribute to vessel loop formation, per se, our data supports a potential role for PCs in the regulation of network patterning. Conversely, networks simulated by the EC-only ABM were thicker, more tortuous, and had more blind-ended branches. This description is consistent with the observed phenotype of pericyte loss in the retina, which is characterized by poorly formed vascular networks [12, 13, 18, 63].

Simonavicius et al. have demonstrated that knockout of endosialin (CD248) in PCs leads to a defect in vascular regression and pruning despite normal recruitment to the EC network in

the mouse retina [19]. Their study suggested that PC-derived endosialin binding to EC-generated (or EC-modified) basement membrane modulated VEGF binding to VEGFR2 – loss of the pathway increased vessel density and loss of normal EC apoptosis during vessel maturation. Taken in context with our ABM findings, these studies suggest that the interplay between ECs and PCs during vascular development in the context of Notch1-DLL4 signaling may in fact be more important than previously thought.

That PCs exert no direct effects on EC signaling was a major assumption of our model. Pedrosa et al. have recently proposed a mechanism by which perivascular cells (PCs and vascular smooth muscle cells) directly interact with the Notch1 signaling axis of developing EC networks, although this was performed in skin wound healing assays, not in the developing retina [64]. Specifically, overexpression of DLL4 led to an increase in PC coverage, decrease in vascular density, and a decrease in vessel leakage as measure by dye extravasation into the extracellular space. Additionally, we simplified EC function by only including signaling via VEGFR and Notch1-DLL4 pathways. The propagation of EC signaling at a network level through Notch1-DLL4 pathways has been described previously [20, 21, 27, 65]. Clearly, Notch1 signaling plays an important role in patterning the developing retinal vasculature. Several other key signaling pathways are implicated in retinal vascular development, including Notch4-EphrinB2 [65] and the bone morphogenic protein family (BMP9 and BMP10) [66]. However, given the current emphasis on VEGF and downstream signaling in treatment for proliferative diabetic retinopathy [14, 16, 67], we felt it prudent to focus on VEGF and Notch signaling. In our ABM, we also simplify the behaviors governing cell-cell contacts by including a rule that states that ECs and PCs must attempt to maintain contact with one another. Notably, this does not allow for the dynamics of EC cadherin expression that has recently been suggested as a mechanism for EC shuffling along angiogenic stalks [68]. Also, the ABM simulations all occurred on a planar surface in 2D – however, given the planar nature of the developing retinal vasculature (particularly at P3 when penetrating branches are rare) [2]. Further, in the planar model environment we excluded pericyte-endothelial cell “overlap” allowing only for pericyte coverage between endothelial cells rather than completely wrapping them (potentially impacting connections to endothelial cells outside the plane of the simulation). Because we do not simulate interactions outside the plane of the ABM we feel that this and the preceding assumptions are valid for the present study.

Our ABM simulations were compared to images of the angiogenic front in P3 murine retinae. This dynamic region of angiogenesis moves across the retina from P0 through approximately P8, and is characterized by ongoing endothelial cell sprouting along astrocytes. We chose to focus our analysis on the dynamics of this region rather than incorporating other network patterning behaviors such as arterio-venous polarization, capillary rarefaction, or formation of deeper retinal vascular layers. Future simulations that incorporate these additional stages of retinal vascular development may further detail the role of PCs in microvascular network patterning. Additionally, binary “all-or-none” comparison between simulations with and without pericytes leaves a great deal of room for further investigation. Simulations to mimic partial knock outs and disease states with reduced, but not complete, pericyte drop-out would be useful to determine the thresholds for pericyte impact on vascular patterning. Indeed, our assumption of coverage based on a 75%

chance of populating pericytes is based on image analysis of postnatal murine retinae and could be further refined through exploration of that parameter space.

The assembly of network structures from heterogeneous components is an ongoing area of intensive research across a broad array of disciplines. For example, Bentley et al. describe self-assembling systems ranging from robotics to vascular biology [69]. In ABMs, the notion of self-assembly is commonly referred to as “emergent behavior” and describes the observation of a behavior that was not explicitly programmed into the model [70, 71]. This is a strength of so-called “bottom-up” approaches to modeling biological phenomena, allowing for a minimal rule set to generate a larger cohort of behaviors [72]. This work represents the first ABM specifically built to understand the interplay of ECs and PCs in the developing retina. Despite the many ocular diseases that are tied to the health of PCs, little has been done to computationally model the direct impact of perivascular cells on endothelial cells in retinal vascular networks undergoing angiogenesis. Our ABM simulations suggest that PCs can exert an effect on EC network patterning without explicitly modifying EC behavior directly through signaling pathways. This possible buffering effect should be taken into account in future studies of EC-PC interactions, particularly those involving active angiogenesis.

Supplementary Material

Refer to Web version on PubMed Central for supplementary material.

Acknowledgments

Funding Support: AHA 13PRE16580001

NIH T32-HL007284

NSF 1235244

NIH 1R01EY022063

NIH 1R00HL105779

We wish to acknowledge AHA grant 13PRE16580001, the Jefferson Trust Big Data Grant, the Cardiovascular Research Center Training Grant NIH T32-HL007284 (to JBW), NSF grant #1235244 (to SMP), NIH 1R01EY022063 (to SMP), the Hartwell Foundation (to SMP), and NIH 1R00HL105779 (to JCC).

References

1. Fruttiger M. Development of the retinal vasculature. Angiogenesis. 2007; 10:77–88. [PubMed: 17322966]
2. Milde F, Lauw S, Koumoutsakos P, Iruela-Arispe ML. The mouse retina in 3D: quantification of vascular growth and remodeling. Integr Biol (Camb). 2013; 5:1426–38. [PubMed: 24136100]
3. Dorrell M, Aguilar E, Friedlander M. Retinal vascular development is mediated by endothelial filopodia, a preexisting astrocytic template and specific R-cadherin adhesion. Investigative ophthalmology & visual. 2002
4. West H, Richardson WD, Fruttiger M. Stabilization of the retinal vascular network by reciprocal feedback between blood vessels and astrocytes. Development. 2005; 132:1855–62. [PubMed: 15790963]

5. Scott A, Powner MB, Gandhi P, Clarkin C, Gutmann DH, Johnson RS, Ferrara N, Fruttiger M. Astrocyte-derived vascular endothelial growth factor stabilizes vessels in the developing retinal vasculature. PLoS One. 2010; 5:e11863. [PubMed: 20686684]
6. Hughes C. Endothelial-stromal interactions in angiogenesis. Current opinion in hematology. 2008; 15:204–209. [PubMed: 18391786]
7. Wisniewska-Kruk J, Hoeben KA, Vogels IM, Gaillard PJ, Van Noorden CJ, Schlingemann RO, Klaassen I. A novel co-culture model of the blood-retinal barrier based on primary retinal endothelial cells, pericytes and astrocytes. Exp Eye Res. 2012; 96:181–90. [PubMed: 22200486]
8. Armulik A, Genove G, Mae M, Nisancioglu MH, Wallgard E, Niaudet C, He L, Norlin J, Lindblom P, Strittmatter K, Johansson BR, Betsholtz C. Pericytes regulate the blood-brain barrier. Nature. 2010; 468:557–61. [PubMed: 20944627]
9. Chang WG, Andrejecsk JW, Kluger MS, Saltzman WM, Pober JS. Pericytes modulate endothelial sprouting. Cardiovasc Res. 2013; 100:492–500. [PubMed: 24042014]
10. Durham JT, Surks HK, Dulmovits BM, Herman IM. Pericyte contractility controls endothelial cell cycle progression and sprouting: insights into angiogenic switch mechanics. Am J Physiol Cell Physiol. 2014; 307:C878–92. [PubMed: 25143350]
11. Stark K, Eckart A, Haidari S, Tirniceriu A, Lorenz M, von Brühl ML, Gärtner F, Khandoga A, Legate K, Pless R, Hepper I, Lauber K, Walzog B, Massberg S. Capillary and arteriolar pericytes attract innate leukocytes exiting through venules and 'instruct' them with pattern-recognition and motility programs. Nature immunology. 2013; 14:41–51. [PubMed: 23179077]
12. Hartnett ME. Pathophysiology and mechanisms of severe retinopathy of prematurity. Ophthalmology. 2015; 122:200–10. [PubMed: 25444347]
13. Wu L, Fernandez-Loaiza P, Sauma J, Hernandez-Bogantes E, Masis M. Classification of diabetic retinopathy and diabetic macular edema. World journal of diabetes. 2013; 4:290–294. [PubMed: 24379919]
14. Hammes HP, Feng Y, Pfister F, Brownlee M. Diabetic retinopathy: targeting vasoregression. Diabetes. 2011; 60:9–16. [PubMed: 21193734]
15. Ejaz S, Chekarova I, Ejaz A, Sohail A, Lim C. Importance of pericytes and mechanisms of pericyte loss during diabetes retinopathy. Diabetes, obesity & metabolism. 2008; 10:53–63.
16. Bandello F, Lattanzio R, Zucchiatti I, Del Turco C. Pathophysiology and treatment of diabetic retinopathy. Acta diabetologica. 2013
17. Cao R, Xue Y, Hedlund EM, Zhong Z, Tritsaris K, Tondelli B, Lucchini F, Zhu Z, Dissing S, Cao Y. VEGFR1-mediated pericyte ablation links VEGF and PlGF to cancer-associated retinopathy. Proc Natl Acad Sci U S A. 2010; 107:856–61. [PubMed: 20080765]
18. Mendel T, Clabough E, Kao D, Demidova-Rice T, Durham J, Zotter B, Seaman S, Cronk S, Rakoczy E, Katz A, Herman I, Peirce S, Yates P. Pericytes derived from adipose-derived stem cells protect against retinal vasculopathy. PloS one. 2013; 8
19. Simonavicius N, Ashenden M, van Weverwijk A, Lax S, Huso D, Buckley C, Huijbers I, Huijber I, Yarwood H, Isacke C. Pericytes promote selective vessel regression to regulate vascular patterning. Blood. 2012; 120:1516–1527. [PubMed: 22740442]
20. Benedito R, Roca C, Sorensen I, Adams S, Gossler A, Fruttiger M, Adams RH. The notch ligands Dll4 and Jagged1 have opposing effects on angiogenesis. Cell. 2009; 137:1124–35. [PubMed: 19524514]
21. Hellstrom M, Phng LK, Hofmann JJ, Wallgard E, Coultas L, Lindblom P, Alva J, Nilsson AK, Karlsson L, Gaiano N, Yoon K, Rossant J, Iruela-Arispe ML, Kalen M, Gerhardt H, Betsholtz C. Dll4 signalling through Notch1 regulates formation of tip cells during angiogenesis. Nature. 2007; 445:776–80. [PubMed: 17259973]
22. Noguera-Troise I, Daly C, Papadopoulos NJ, Coetzee S, Boland P, Gale NW, Lin HC, Yancopoulos GD, Thurston G. Blockade of Dll4 inhibits tumour growth by promoting non-productive angiogenesis. Nature. 2006; 444:1032–7. [PubMed: 17183313]
23. Chappell JC, Wiley DM, Bautch VL. Regulation of blood vessel sprouting. Seminars in cell & developmental biology. 2011; 22:1005–11. [PubMed: 22020130]
24. Chappell JC, Taylor SM, Ferrara N, Bautch VL. Local guidance of emerging vessel sprouts requires soluble Flt-1. Developmental cell. 2009; 17:377–86. [PubMed: 19758562]

25. Carlier A, Geris L, Bentley K, Carmeliet G, Carmeliet P, Van Oosterwyck H. MOSAIC: a multiscale model of osteogenesis and sprouting angiogenesis with lateral inhibition of endothelial cells. PLoS computational biology. 2012; 8
26. Jakobsson L, Franco C, Bentley K, Collins R, Ponsioen B, Aspalter I, Rosewell I, Busse M, Thurston G, Medvinsky A, Schulte-Merker S, Gerhardt H. Endothelial cells dynamically compete for the tip cell position during angiogenic sprouting. Nature cell biology. 2010; 12:943–953. [PubMed: 20871601]
27. Bentley K, Gerhardt H, Bates PA. Agent-based simulation of notch-mediated tip cell selection in angiogenic sprout initialisation. Journal of theoretical biology. 2008; 250:25–36. [PubMed: 18028963]
28. Hashambhoy YL, Chappell JC, Peirce SM, Bautch VL, Mac Gabhann F. Computational modeling of interacting VEGF and soluble VEGF receptor concentration gradients. Frontiers in physiology. 2011; 2:62. [PubMed: 22007175]
29. Kleinstreuer N, Dix D, Rountree M, Baker N, Sipes N, Reif D, Spencer R, Knudsen T. A computational model predicting disruption of blood vessel development. PLoS computational biology. 2013:9.
30. Fong G, Rossant J, Gertsenstein M, Breitman M. Role of the Flt-1 receptor tyrosine kinase in regulating the assembly of vascular endothelium. Nature. 1995; 376:66–70. [PubMed: 7596436]
31. Michielsen K, De Raedt H. Integral-geometry morphological image analysis. Physics Reports. 2001; 347:461–538.
32. Taylor AC, Seltz LM, Yates PA, Peirce SM. Chronic whole-body hypoxia induces intussusceptive angiogenesis and microvascular remodeling in the mouse retina. Microvasc Res. 79:93–101. [PubMed: 20080108]
33. Claybon A, Bishop AJ. Dissection of a mouse eye for a whole mount of the retinal pigment epithelium. J Vis Exp. 2011
34. Gerhardt H, Betsholtz C. Endothelial-pericyte interactions in angiogenesis. Cell Tissue Res. 2003; 314:15–23. [PubMed: 12883993]
35. MATLAB and Statistics Toolbox R2012b. Natick, Massachusetts: MathWorks Inc.;
36. Wilensky, U. Netlogo. Center for Connected Learning and Computer-Based Modeling, Northwestern University; Evanston, IL: 1999. http://ccl.northwestern.edu/netlogo
37. Adamson R. Microvascular endothelial cell shape and size in situ. Microvascular research. 1993; 46:77–88. [PubMed: 8412854]
38. Roca C, Adams RH. Regulation of vascular morphogenesis by Notch signaling. Genes Dev. 2007; 21:2511–24. [PubMed: 17938237]
39. Wieisstein, EW. Moore Neighborhood. 2017. [MathWorld - A Wolfram Web Resource] http://mathworld.wolfram.com/MooreNeighborhood.html
40. Gillespie DT. Exact Stochastic Simulation of Coupled Chemical-Reactions. Journal of Physical Chemistry. 1977; 81:2340–2361.
41. Mac Gabhann F, Yang MT, Popel AS. Monte Carlo simulations of VEGF binding to cell surface receptors in vitro. Biochim Biophys Acta. 2005; 1746:95–107. [PubMed: 16257459]
42. Gillespie DT. Stochastic simulation of chemical kinetics. Annu Rev Phys Chem. 2007; 58:35–55. [PubMed: 17037977]
43. Lecca P. Stochastic chemical kinetics: A review of the modelling and simulation approaches. Biophys Rev. 2013; 5:323–345. [PubMed: 28510113]
44. Gridley T. Notch signaling in the vasculature. Curr Top Dev Biol. 2010; 92:277–309. [PubMed: 20816399]
45. Chappell JC, Wiley DM, Bautch VL. Regulation of blood vessel sprouting. Semin Cell Dev Biol. 2011; 22:1005–11. [PubMed: 22020130]
46. Herbert SP, Stainier DY. Molecular control of endothelial cell behaviour during blood vessel morphogenesis. Nat Rev Mol Cell Biol. 2011; 12:551–64. [PubMed: 21860391]
47. Carmeliet P, Lampugnani MG, Moons L, Breviario F, Compernolle V, Bono F, Balconi G, Spagnuolo R, Oosthuyse B, Dewerchin M, Zanetti A, Angellilo A, Mattot V, Nuyens D, Lutgens E, Clotman F, de Ruiter MC, Gittenberger-de Groot A, Poelmann R, Lupu F, Herbert JM, Collen

D, Dejana E. Targeted deficiency or cytosolic truncation of the VE-cadherin gene in mice impairs VEGF-mediated endothelial survival and angiogenesis. Cell. 1999; 98:147–57. [PubMed: 10428027]

48. Carmeliet P, Collen D. Molecular basis of angiogenesis. Role of VEGF and VE-cadherin. Ann N Y Acad Sci. 2000; 902:249–62. discussion 262-4. [PubMed: 10865845]
49. Gerhardt H, Golding M, Fruttiger M, Ruhrberg C, Lundkvist A, Abramsson A, Jeltsch M, Mitchell C, Alitalo K, Shima D, Betsholtz C. VEGF guides angiogenic sprouting utilizing endothelial tip cell filopodia. J Cell Biol. 2003; 161:1163–77. [PubMed: 12810700]
50. Arima S, Nishiyama K, Ko T, Arima Y, Hakozaki Y, Sugihara K, Koseki H, Uchijima Y, Kurihara Y, Kurihara H. Angiogenic morphogenesis driven by dynamic and heterogeneous collective endothelial cell movement. Development. 2011; 138:4763–76. [PubMed: 21965612]
51. Silva EA, Mooney DJ. Effects of VEGF temporal and spatial presentation on angiogenesis. Biomaterials. 2010; 31:1235–41. [PubMed: 19906422]
52. Anderson EM, Mooney DJ. The Combination of Vascular Endothelial Growth Factor and Stromal Cell-Derived Factor Induces Superior Angiogenic Sprouting by Outgrowth Endothelial Cells. J Vasc Res. 2015; 52:62–9. [PubMed: 26045306]
53. Du Y, Herath SC, Wang QG, Wang DA, Asada HH, Chen PC. Three-Dimensional Characterization of Mechanical Interactions between Endothelial Cells and Extracellular Matrix during Angiogenic Sprouting. Sci Rep. 2016; 6:21362. [PubMed: 26903154]
54. Costa G, Harrington KI, Lovegrove HE, Page DJ, Chakravartula S, Bentley K, Herbert SP. Asymmetric division coordinates collective cell migration in angiogenesis. Nat Cell Biol. 2016; 18:1292–1301. [PubMed: 27870831]
55. Kelly-Goss M, Sweat R, Stapor P, Peirce S, Murfee W. Targeting Pericytes for Angiogenic Therapies. Microcirculation (New York, NY: 1994). 2013
56. Scheef E, Sorenson C, Sheibani N. Attenuation of proliferation and migration of retinal pericytes in the absence of thrombospondin-1. American journal of physiology Cell physiology. 2009; 296:34.
57. Ribatti D, Nico B, Crivellato E. The role of pericytes in angiogenesis. The International journal of developmental biology. 2011; 55:261–268. [PubMed: 21710434]
58. Díaz-Flores L, Gutiérrez R, Varela H, Rancel N, Valladares F. Microvascular pericytes: a review of their morphological and functional characteristics. Histology and histopathology. 1991; 6:269–286. [PubMed: 1802127]
59. Armulik A, Genové G, Betsholtz C. Pericytes: developmental, physiological, and pathological perspectives, problems, and promises. Developmental cell. 2011; 21:193–215. [PubMed: 21839917]
60. Kim J, Oh WJ, Gaiano N, Yoshida Y, Gu C. Semaphorin 3E-Plexin-D1 signaling regulates VEGF function in developmental angiogenesis via a feedback mechanism. Genes Dev. 2011; 25:1399–411. [PubMed: 21724832]
61. Hofmann JJ, Luisa Iruela-Arispe M. Notch expression patterns in the retina: An eye on receptor-ligand distribution during angiogenesis. Gene Expr Patterns. 2007; 7:461–70. [PubMed: 17161657]
62. Stenzel D, Franco CA, Estrach S, Mettouchi A, Sauvaget D, Rosewell I, Schertel A, Armer H, Domogatskaya A, Rodin S, Tryggvason K, Collinson L, Sorokin L, Gerhardt H. Endothelial basement membrane limits tip cell formation by inducing Dll4/Notch signalling in vivo. EMBO Rep. 2011; 12:1135–43. [PubMed: 21979816]
63. Motiejunaite R, Kazlauskas A. Pericytes and ocular diseases. Exp Eye Res. 2008; 86:171–7. [PubMed: 18078933]
64. Pedrosa AR, Trindade A, Fernandes AC, Carvalho C, Gigante J, Tavares AT, Dieguez-Hurtado R, Yagita H, Adams RH, Duarte A. Endothelial Jagged1 Antagonizes Dll4 Regulation of Endothelial Branching and Promotes Vascular Maturation Downstream of Dll4/Notch1. Arterioscler Thromb Vasc Biol. 2015
65. Hainaud P, Contreres JO, Villemain A, Liu LX, Plouet J, Tobelem G, Dupuy E. The role of the vascular endothelial growth factor-Delta-like 4 ligand/Notch4-ephrin B2 cascade in tumor vessel remodeling and endothelial cell functions. Cancer Res. 2006; 66:8501–10. [PubMed: 16951162]

66. Ricard N, Ciais D, Levet S, Subileau M, Mallet C, Zimmers TA, Lee SJ, Bidart M, Feige JJ, Bailly S. BMP9 and BMP10 are critical for postnatal retinal vascular remodeling. Blood. 2012; 119:6162–71. [PubMed: 22566602]

67. Bressler S, Qin H, Melia M, Bressler N, Beck R, Chan C, Grover S, Miller D. N. Diabetic Retinopathy Clinical Research. Exploratory analysis of the effect of intravitreal ranibizumab or triamcinolone on worsening of diabetic retinopathy in a randomized clinical trial. JAMA ophthalmology. 2013; 131:1033–1040. [PubMed: 23807371]

68. Bentley K, Franco CA, Philippides A, Blanco R, Dierkes M, Gebala V, Stanchi F, Jones M, Aspalter IM, Cagna G, Westrom S, Claesson-Welsh L, Vestweber D, Gerhardt H. The role of differential VE-cadherin dynamics in cell rearrangement during angiogenesis. Nat Cell Biol. 2014; 16:309–21. [PubMed: 24658686]

69. Bentley K, Philippides A, Ravasz Regan E. Do endothelial cells dream of eclectic shape? Dev Cell. 2014; 29:146–58. [PubMed: 24780735]

70. Borlin CS, Lang V, Hamacher-Brady A, Brady NR. Agent-based modeling of autophagy reveals emergent regulatory behavior of spatio-temporal autophagy dynamics. Cell Commun Signal. 2014; 12:56. [PubMed: 25214434]

71. Thorne BC, Hayenga HN, Humphrey JD, Peirce SM. Toward a multi-scale computational model of arterial adaptation in hypertension: verification of a multi-cell agent based model. Frontiers in physiology. 2011; 2:20. [PubMed: 21720536]

72. Walpole J, Papin JA, Peirce SM. Multiscale computational models of complex biological systems. Annu Rev Biomed Eng. 2013; 15:137–54. [PubMed: 23642247]

73. Barkefors I, Le Jan S, Jakobsson L, Hejll E, Carlson G, Johansson H, Jarvius J, Park JW, Li Jeon N, Kreuger J. Endothelial cell migration in stable gradients of vascular endothelial growth factor A and fibroblast growth factor 2: effects on chemotaxis and chemokinesis. J Biol Chem. 2008; 283:13905–12. [PubMed: 18347025]

74. Liu L, Ratner BD, Sage EH, Jiang S. Endothelial cell migration on surface-density gradients of fibronectin, VEGF, or both proteins. Langmuir. 2007; 23:11168–73. [PubMed: 17892312]

75. van der Meer AD, Vermeul K, Poot AA, Feijen J, Vermes I. A microfluidic wound-healing assay for quantifying endothelial cell migration. Am J Physiol Heart Circ Physiol. 2010; 298:H719–25. [PubMed: 19933413]

76. Stefanini MO, Wu FT, Mac Gabhann F, Popel AS. A compartment model of VEGF distribution in blood, healthy and diseased tissues. BMC Syst Biol. 2008; 2:77. [PubMed: 18713470]

Perspectives

The underpinnings of angiogenesis are developmental pathways that are called upon during tissue growth, development, and repair. Understanding how multiple cell types interact to control angiogenic growth has implication for tissue repair and engineering, but also aids in understanding how these same pathways give rise to proliferative vascular diseases such as diabetic retinopathy and tumorigenesis. Our results suggest a role for perivascular cells in retinal angiogenesis which impacts the formation of endothelial cell networks, potentially guiding the shape and function of vascular beds at the very outset of endothelial sprouting.

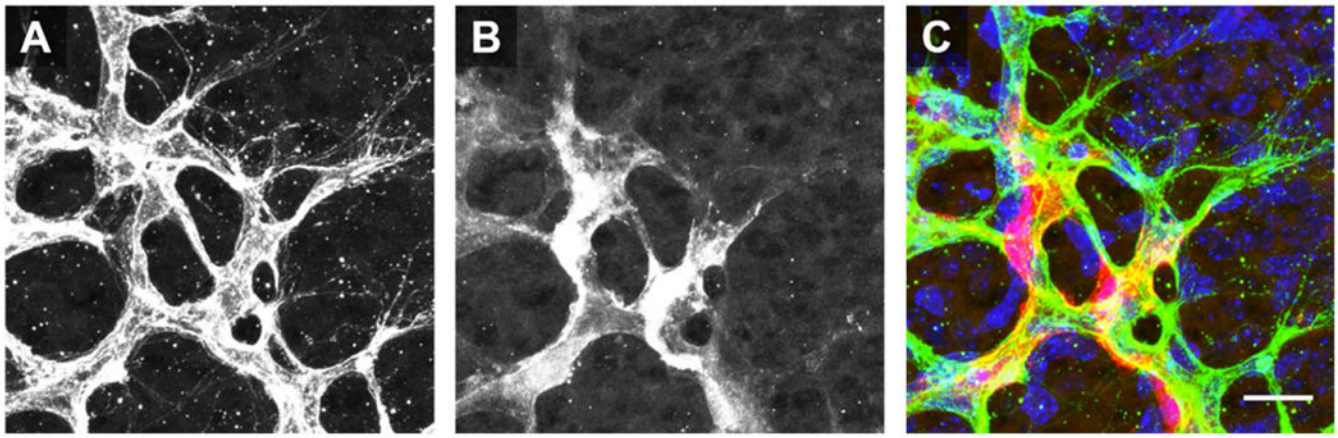

Figure 1. Pericytes are Closely Associated with Endothelial Cells at the Angiogenic Front

Images of ECs (A, PECAM) and PCs (B, NG2) at the angiogenic front. Pseudocolor overlay (C) demonstrates that the cell bodies of PCs (red) are in direct contact with ECs (green) in regions of active angiogenic sprout formation (nuclei shown in Blue, DAPI). Scale bar: 20 microns.

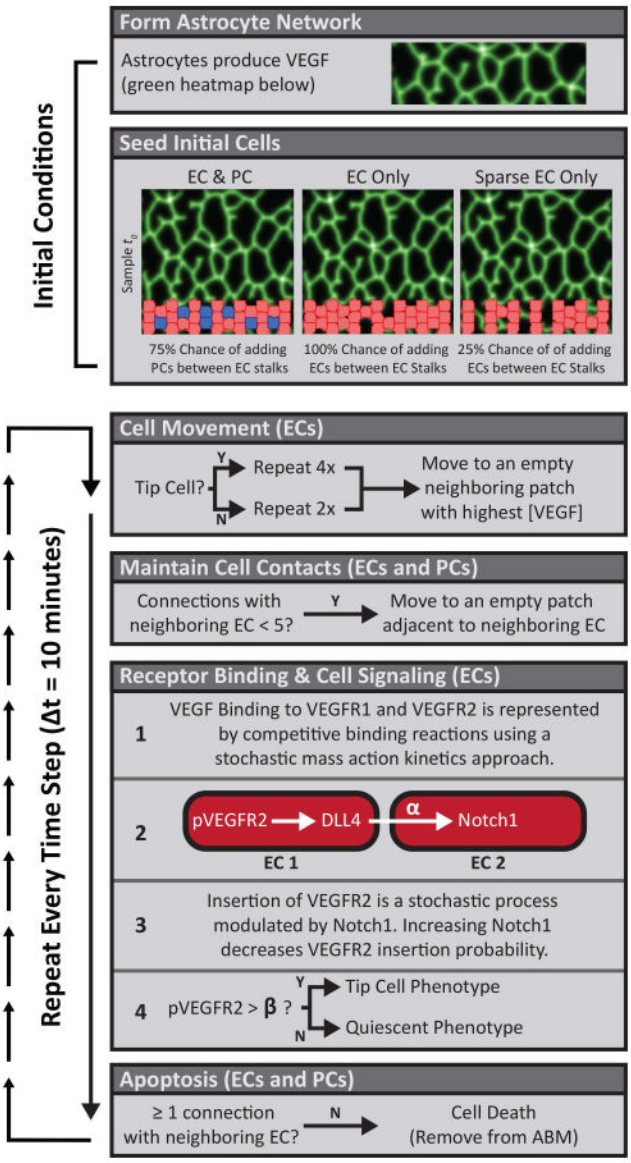

Figure 2. Retinal ABM Process Diagram

Formation of the astrocyte network (Figure S1) and initial cell seeding are performed as part of the initial conditions at the beginning of each simulation. Cell movement, maintenance of cell contacts, receptor binding, and cell signaling occur at each time step (highlighted in orange). Simulations are run for a total of 80 time steps after which EC locations are saved as tif images for Minkowski analysis. ECs and PCs are represented in red and blue, respectively.

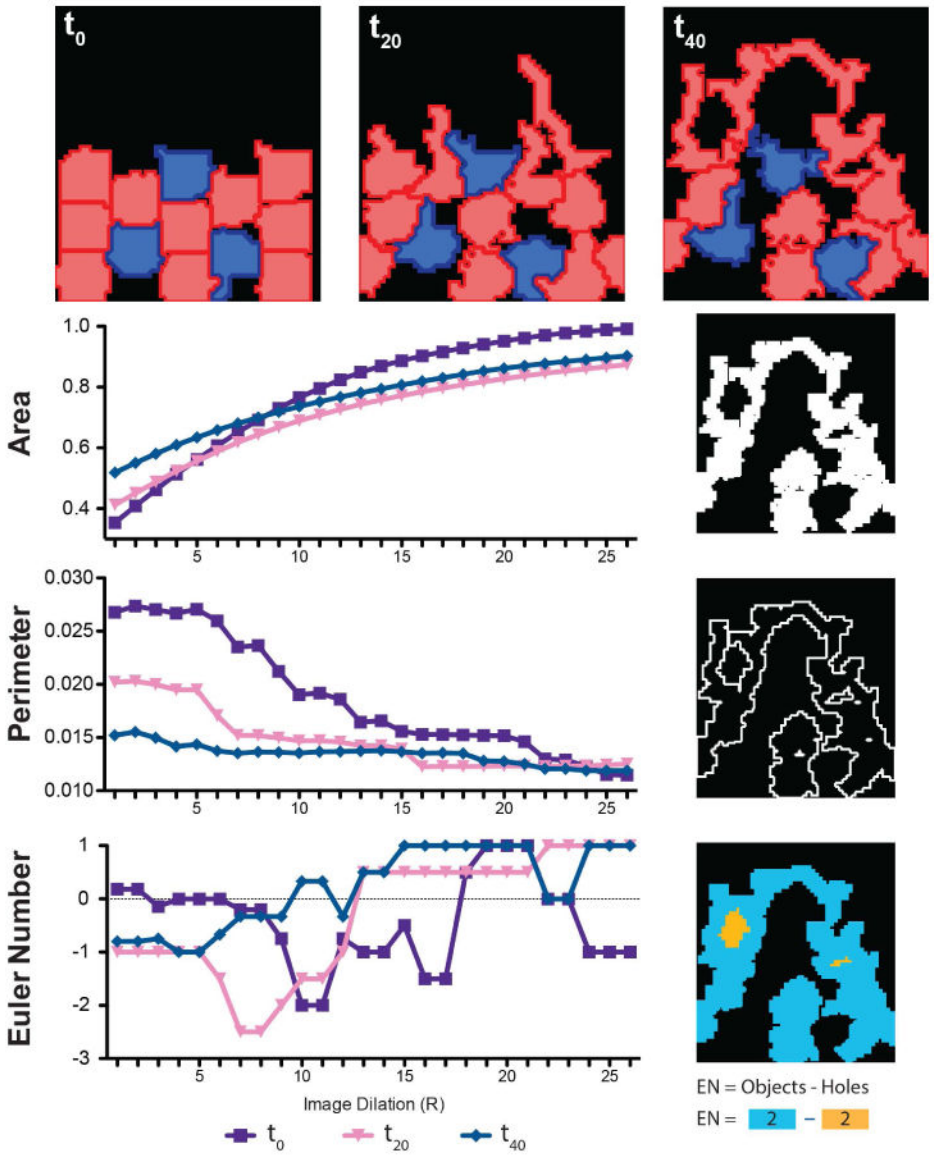

Figure 3. Illustrative Timecourse of ABM Output and Minkowski Analysis

Model output (representative image of a single simulation) from a network of 10 ECs (red) and 3 PCs (blue) over 3.3 hours demonstrating extension of the vascular front over time. Minkowsky Functionals corresponding to these images are shown below to illustrate the unique shape of these curves as a function vascular network geometry.

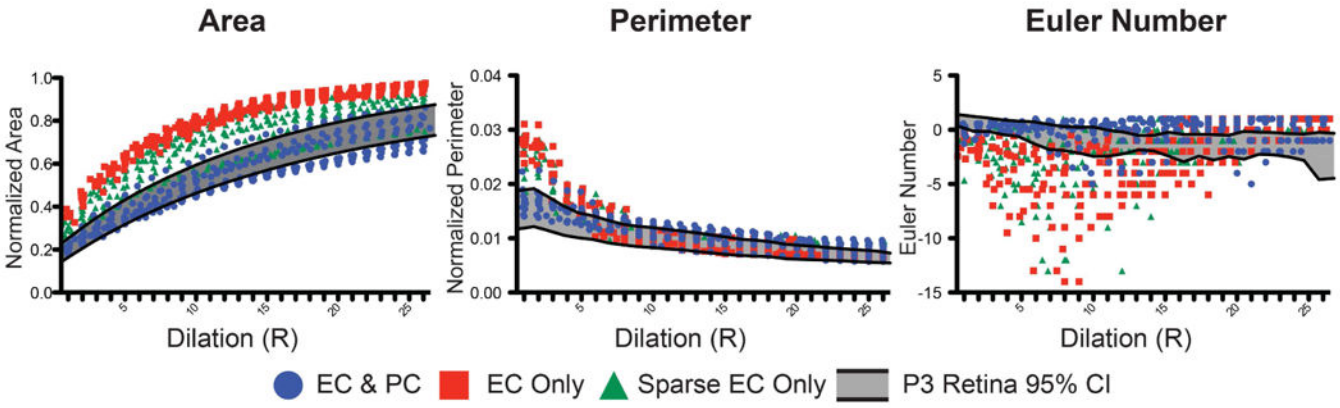

Figure 4. Comparison of ABM-generated Minkowski Functionals to Minkowski Functionals from Actual P3 Retinae

(A) Minkowski functionals of a single parameter combination (α=20,β=30) as compared to 95% confidence intervals of p3 retinas(shaded region) over a range of image dilation values (N = 10 ABM simulations, N = 9 P3 retinal wings). (B) The percentage of data points within the shaded region for each simulation type corresponds to the scoring metric.

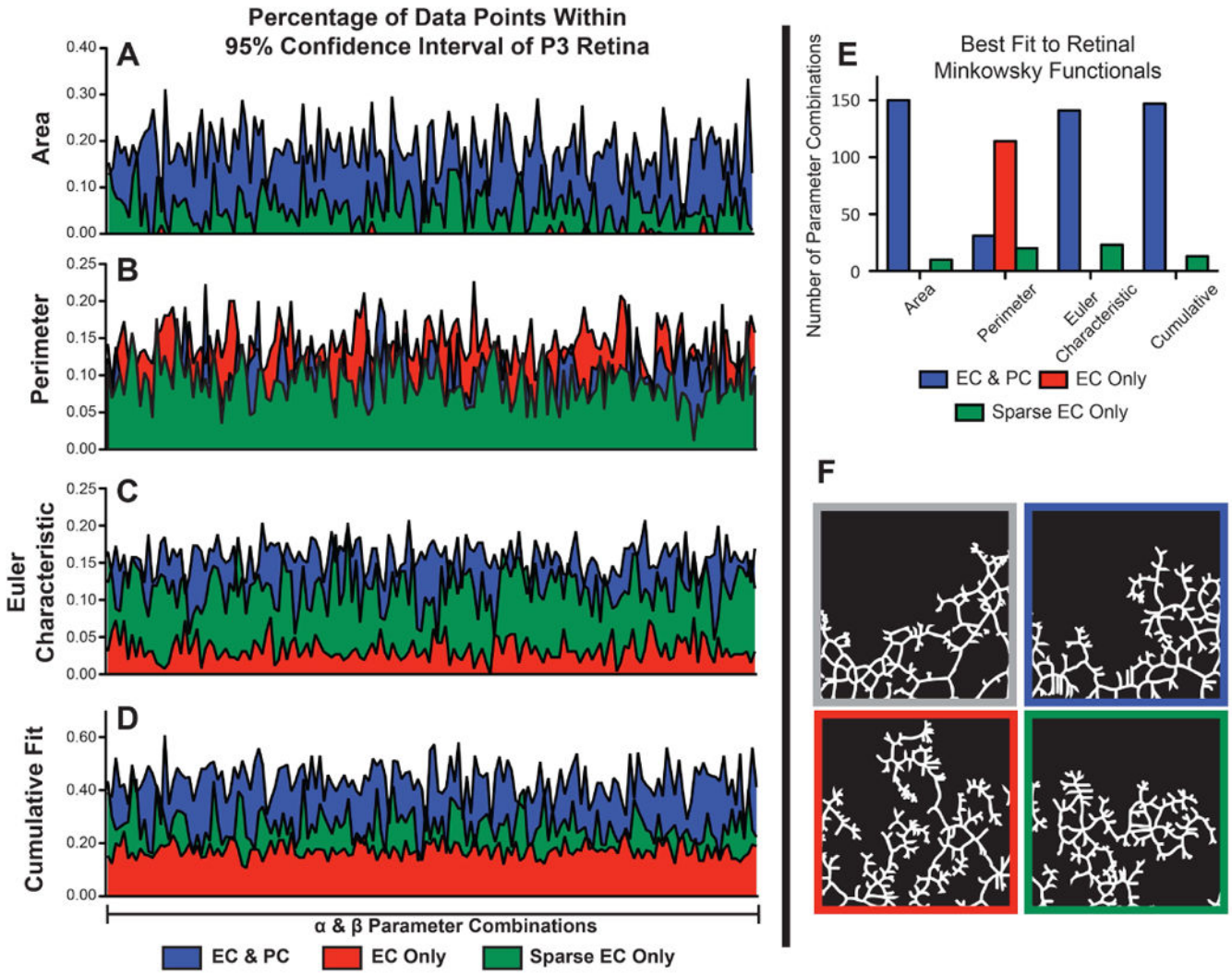

Figure 5. Simulations that Include Pericytes Outperform those without Pericytes Based on Comparison between ABM-Generated and Observed P3 Retinae Minkowski Functionals

Minkowski functionals (Area (A), Perimeter (B), and Euler Characteristic (C)) were calculated from the positions of ECs at the final time step of the ABM for 160 combination of α and β parameters.The fraction of ABM-generated data points falling within the 95% confidence interval of the Minkowski functionals for P3 retinas is plotted as a function of parameter combinations for each of the experimental conditions. Cumulative Fit (D) is the fraction of all ABM data points falling within the 95% confidence interval of P3 retina data across all three Minkowski Functionals. (E) Total number of parameter combinations for which each simulation type had the best match to P3 retina data (e.g. most points within the P3 Retinal 95% CI) as individual Minkowski functionals or cumulatively. (F) Skeletonized binary images used for the Minkowski analysis, clockwise from top left: exemplar P3 Retina immunohistochemical stained ECs, ABM with ECs & PCs, ABM with sparsely populated ECs, ABM with only ECs. N = 10 ABM simulations per parameter combination, N = 9 P3 retinal wings.

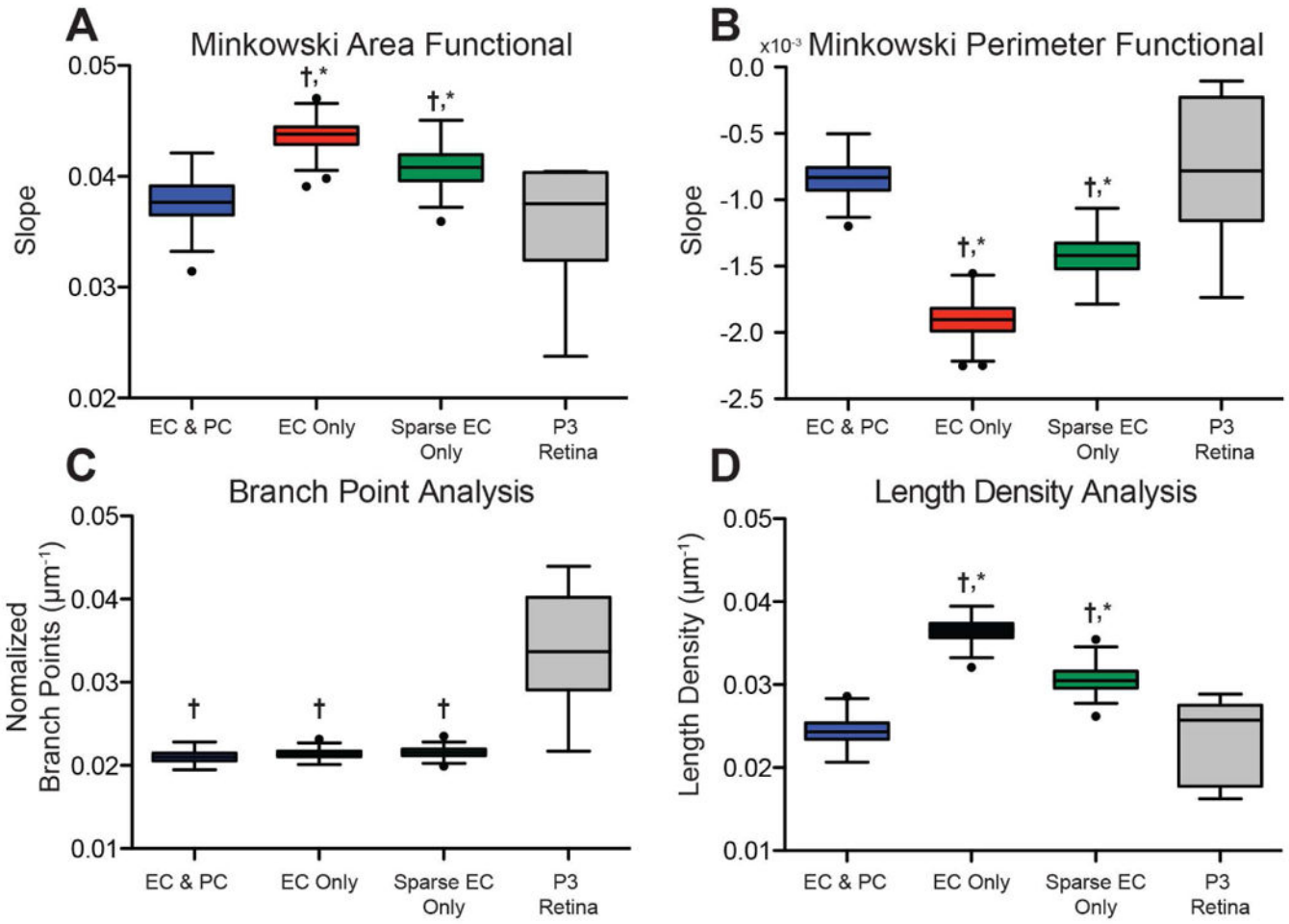

Figure 6. ABM Simulations with PCs Share Vessel Network Properties with Observed P3 Retinae

(A, B) Slopes for AREA and PERIMETER functionals were significantly different when comparing either EC Only or Sparse EC Only to simulations with pericytes(*,$P<0.01$) or P3 retina data (†,$P<0.01$).(c) The number of branch points per endothelial cell area was significantly less for all ABM simulations when compared to P3 retina data (†,$P<0.01$). (D)Simulations without pericytes (EC Only and Sparse EC Only) had significantly more length density as compared to both ABM simulations with pericytes (*, $P<0.01$) and P3 retina data (†,$P<0.01$). N = 10 ABM simulations, N = 9 P3 retinal wings,Tukey Box Plots with outliers shown as black circles).

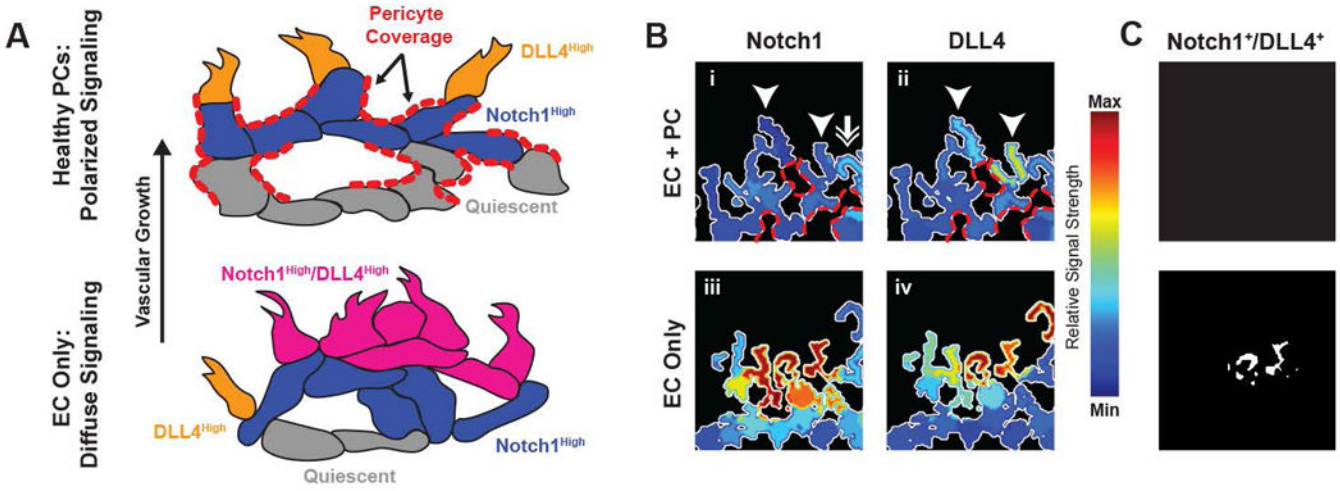

Figure 7. Proposed Model for PC Signal Buffering: Notch1-DLL4 EC Signal Polarity is Lost and Becomes Diffuse in Simulations with Only ECs

(A) Proposed model of pericyte buffering effect whereby EC-EC intercellular connections are limited by the presence of PCs, disrupting normal Notch1-DLL4 polarity. PC coverage is highlighted in red dashes and prohibits ECs from making additional connections. In the case without PCs, a population of Notch1High/DLL4High cells disrupts the normal polarity of the angiogenic front. (B) Notch1 and DLL4 activity in simulations with and without PCs. Pericyte contact locations are highlighted with red dashes. Arrowheads indicate a DLL4 "high" EC with neighboring Notch1 "high" EC (double arrow). Heatmap is relative signal strength of Notch1 or DLL4 as compared to ECs from both displayed simulations. (C) Cells double positive for Notch1 and DLL4 high levels of expression; in the EC Only simulations there are several Notch1^{+}/DLL4^{+} Cells.

Table 1

ABM Parameter Values

Parameter	Description	Value	Reference
EC_{SA}	*EC Surface Area*	968 μm^2	[37]
EC_{ctx}	*Chemotactic Migration Rate*	30 μm·h^{-1}	Estimated from [73-75]
α	*Notch Transfer Coefficient*	Model Specific	n/a
β	*Tip Cell Activation Threshold*	Model Specific	n/a
k_{on}^{R2}	*VEGF binding to VEGFR2*	1.0E7 M^{-1}s^{-1}	[76]
k_{on}^{R1}	*VEGF binding to VEGFR1*	3.0E7 M^{-1}s^{-1}	[76]
k_{off}^{R2}	*VEGF dissociation from VEGFR2*	1.0E-3 s^{-1}	[76]
k_{off}^{R1}	*VEGF dissociation from VEGFR1*	1.0E-3 s^{-1}	[76]
k_{int}	*Internalization rate of VEGFR2*	2.8E-4 s^{-1}	[76]